

Time-Resolved In Situ Measurements During Rapid Alloy Solidification: Experimental Insight for Additive Manufacturing

JOSEPH T. MCKEOWN,^{1,5} KAI ZWEIACKER,² CAN LIU,² DANIEL R. COUGHLIN,³ AMY J. CLARKE,³ J. KEVIN BALDWIN,⁴ JOHN W. GIBBS,³ JOHN D. ROEHLING,¹ SETH D. IMHOFF,³ PAUL J. GIBBS,³ DAMIEN TOURET,³ JÖRG M.K. WIEZOREK,² and GEOFFREY H. CAMPBELL¹

1.—Materials Science Division, Lawrence Livermore National Laboratory, Livermore, CA 94550, USA. 2.—Department of Mechanical Engineering and Materials Science, University of Pittsburgh, Pittsburgh, PA 15261, USA. 3.—Materials Science and Technology Division, Los Alamos National Laboratory, Los Alamos, NM 87545, USA. 4.—Center for Integrated Nanotechnologies, Los Alamos National Laboratory, Los Alamos, NM 87545, USA. 5.—e-mail: mckeown3@llnl.gov

Additive manufacturing (AM) of metals and alloys is becoming a pervasive technology in both research and industrial environments, though significant challenges remain before widespread implementation of AM can be realized. In situ investigations of rapid alloy solidification with high spatial and temporal resolutions can provide unique experimental insight into microstructure evolution and kinetics that are relevant for AM processing. Hypoeutectic thin-film Al–Cu and Al–Si alloys were investigated using dynamic transmission electron microscopy to monitor pulsed-laser-induced rapid solidification across microsecond timescales. Solid–liquid interface velocities measured from time-resolved images revealed accelerating solidification fronts in both alloys. The observed microstructure evolution, solidification product, and presence of a morphological instability at the solid–liquid interface in the Al–4 at.%Cu alloy are related to the measured interface velocities and small differences in composition that affect the thermophysical properties of the alloys. These time-resolved in situ measurements can inform and validate predictive modeling efforts for AM.

INTRODUCTION

The production of complex metal and alloy components using additive manufacturing (AM) techniques represents a drastic departure from traditional manufacturing processes. However, while AM is poised to completely alter the design and production of metallic parts across a broad spectrum of industries, fundamental scientific challenges remain before AM can be fully realized as a transformative technology. One of the most serious challenges to wide-ranging adoption of AM to metals is qualification, where concern is mainly focused on quality of the additively manufactured material.^{1,2} Enabling qualification requires physical understanding of the materials science of the AM process across broad length and timescales.

Components prepared by AM often exhibit microstructures and properties that differ significantly from those of conventional cast and wrought alloy components. Of critical importance to AM processes is an understanding of processing–microstructure–properties/performance relationships. Much effort toward understanding these relationships has been focused on modeling various aspects of AM^{1,3–11}—largely aimed at laser–materials interactions, melt pool physics, process maps, microstructure and mechanical properties predictions, and residual stress (with somewhat limited experimental input with regard to these modeling efforts), for example. Predictive modeling capabilities are critical and provide a mechanism to develop a comprehensive understanding of AM processes, but models must be informed and validated by experimental data.

In the case of selective laser melting (SLM) using metal and alloy powders, the microstructures that develop during AM result from rapid solidification, an inherently non-equilibrium process. Microstructural spatial scales, metastable phase formation, compositional segregation, distribution of phases, and crystallographic texture are all factors that can vary greatly as the solid-liquid transformation front is driven further from equilibrium.¹² The properties and performance of additively manufactured components will be dictated by the microstructures that develop for a given composition and thermal history, beginning with the rapid solidification process. Understanding the microstructure evolution and kinetics of these far-from-equilibrium phase transformations at the requisite timescales is therefore essential, and in situ studies of rapid solidification therefore have significant scientific and technological implications for AM.

Accessing the temporal regimes over which rapid solidification occurs with in situ characterization techniques has proved challenging experimentally, due to the extremely high cooling rates ($\sim 10^5$ – 10^7 K/s) and resultant solidification front velocities ($\sim 10^{-2}$ – 10^2 m/s) experienced during rapid solidification.^{13–17} We use time-resolved, in situ multi-frame transmission electron microscopy in this work to directly image the solidification front and its evolution during rapid solidification in thin-film Al–Cu and Al–Si alloys. These alloys both contain eutectics in the Al-rich portions of the equilibrium phase diagrams,^{18,19} with eutectic temperatures/compositions of 548°C/ ~ 17 at.%Cu (~ 32 wt.%Cu) and 577°C/ ~ 12 at.%Si (~ 12 wt.%Si) for, respectively, the Al–Cu/Si systems. The Al–Cu eutectic consists of terminal phases of α -Al and the ordered intermetallic θ -Al₂Cu phase with a composition of ~ 33 at.%Cu (~ 54 wt.%Cu); the Al–Si eutectic spans the entire composition range and consists of α -Al and pure Si. These alloys serve as model materials systems due to the availability of well-defined thermo-physical data^{20–26} that exist and numerous ex situ studies of the microstructures that develop in rapidly solidified Al–Cu^{27–34} and Al–Si^{24,35–38} alloys.

The dynamics of rapid solidification in pure Al¹⁶ and hypoeutectic Al–Cu¹⁷ alloy thin films were previously characterized in situ using the dynamic transmission electron microscope (DTEM)^{16,17,39–43} at Lawrence Livermore National Laboratory in single-shot mode, allowing acquisition of a single image at a specified delay time after a pulsed-laser melting event. The DTEM instrument now operates in Movie Mode,^{44,45} a single-shot, multiple-image acquisition mode that permits the study of microstructural evolution and kinetics in far greater detail by allowing for acquisition of up to 9 images with user-defined delay times after a pulsed-laser melting event. Movie mode DTEM provides higher data throughput and a reduction in uncertainty and experimental error while following the dynamics of complex, irreversible processes such as rapid solidification. Here, we present results of in situ movie

mode DTEM investigations of rapid solidification in thin-film, hypoeutectic Al–4 at.%Cu (Al–4Cu) and Al–3 at.%Si (Al–3Si) alloys. This experimental approach can be extended to other types of alloy systems and is important for the development of improved, validated predictive modeling capabilities for AM and, more generally, non-equilibrium materials processing.

EXPERIMENTAL

Sample Preparation and Characterization

Al–4 at.%Cu (Al–4Cu) thin films were deposited on 50-nm-thick silicon nitride support film TEM grids (Ted Pella) at room temperature by dual electron beam evaporation (Pascal Technologies Dual E-Beam Deposition System). The typical base vacuum in the chamber before deposition was $< 5 \times 10^{-8}$ Torr, and the evaporation rate was maintained between 2 nm/s and 2.5 nm/s. Surface profilometry confirmed the film thickness of 80 nm and the chemical composition of the films was measured utilizing a JEOL JEM2100F TEM/STEM operated at 200 kV and equipped with an energy-dispersive spectroscopy (EDS) detector. The as-deposited Al–4Cu films were nanocrystalline with an average grain size of ~ 50 nm.

Al–3 at.%Si thin films were deposited on 50-nm-thick silicon nitride support film TEM grids (Ted Pella) and PELCO[®] 6–8 layer graphene TEM support films on lacey carbon, 300-mesh copper grids (Ted Pella) using dc magnetron sputtering in a chamber with a base pressure of $< 5 \times 10^{-8}$ Torr. The process pressure was 3.3×10^{-3} Torr. The main sputter target was Al–1 wt.%Si, run using a power of 300 W, with a secondary Si target to increase the Si content, run using a power of 10 W. Chemical compositions of the depositions on lacey carbon were measured utilizing a FEI Tecnai Analytical TEM/STEM operated at 300 kV and equipped with an EDS detector. All the as-deposited Al–3Si films were nanocrystalline.

Post-mortem microstructure characterization of the rapidly solidified Al–Cu and Al–Si microstructures using high-angle annular dark-field scanning transmission electron microscopy (HAADF STEM) was conducted in a JEOL JEM-2010F TEM/STEM instrument operated at 200 kV and a FEI Tecnai Analytical TEM/STEM operated at 300 kV.

Time-Resolved Transmission Electron Microscopy

In situ rapid solidification experiments were conducted in the DTEM operating at 200 kV in movie mode, which allows acquisition of 9 frames with user-controlled exposure times per frame and inter-frame temporal spacings from a single drive laser (melting) event. The thermal stimulus for melting was provided using a 1064-nm wavelength, ~ 15 -ns pulsed Nd:YAG laser with a

Gaussian beam profile ($1/e^2$ diameter of $135 \pm 5 \mu\text{m}$) incident at 45° to the alloy thin films and laser pulse fluences of $\sim 530 \pm 40 \text{ mJ/cm}^2$ and $\sim 580 \pm 40 \text{ mJ/cm}^2$ for, respectively, the Al–4Cu and Al–3Si alloys. Photo-emitted electron pulses were generated with a fiber-based Nd:YAG laser converted to 5th harmonic (213 nm) incident on a Ta disk that serves as a photocathode in the DTEM. Imaging of the solidification dynamics was performed with a 50-ns duration electron pulse, which represents exposure time per frame and thus the temporal resolution of the DTEM imaging experiments. An electrostatic deflector installed beneath the electron optics in the TEM column shifts each frame to a different part of a $2 \text{ k} \times 2 \text{ k}$ CCD camera with single-electron detection sensitivity, allowing acquisition of the 9 frames in a single exposure of the CCD camera while circumventing the $\sim\text{ms}$ temporal limit on the refresh rate of the camera. Thus, each acquisition is a $2 \text{ k} \times 2 \text{ k}$ image that is divided into 9 frames of approximately equal size.

User-defined pulse trains were chosen, depending on the data to be acquired, to image the rapid solidification processes at different magnifications. Low-magnification imaging allowed observation of the entire melt pool in the field of view of each of the 9 frames with intrinsic spatial resolutions of $\sim 148 \text{ nm/pixel}$ and $\sim 173 \text{ nm/pixel}$ for experiments with, respectively, Al–4Cu and Al–3Si. These images provided measurements of solidification front velocities and overall microstructure evolution during rapid solidification. Low-magnification experiments were conducted with a $2.5\text{-}\mu\text{s}$ inter-frame temporal spacing. Higher-magnification imaging allowed for observation of various growth modes at specific locations along the solid–liquid interface across time intervals identified by low-magnification imaging experiments. Higher-magnification experiments were conducted using $0.5\text{-}\mu\text{s}$ and $1.0\text{-}\mu\text{s}$ inter-frame temporal spacings for, respectively, Al–4Cu and Al–3Si, and images were acquired with an intrinsic spatial resolution of $\sim 17.3 \text{ nm/pixel}$.

Image Analysis for Velocity Measurements

Solidification front velocities were measured directly from the low-magnification time-delay images. Quantitative measurements of the area and semi-major, r_a , and semi-minor, r_b , axes of the elliptical melt pool were performed using ImageJ.^{46,47} The shapes of the melt pools are elliptical as a result of the 45° angle of incidence of the Gaussian laser pulse relative to the film normal. The measurements of the axes of the melt pool were determined with errors of $\pm 450 \text{ nm}$ and $\pm 520 \text{ nm}$, respectively, for Al–4Cu and Al–3Si, corresponding to an absolute error range of ~ 6 pixels. Error bars on plots of the melt pool areas and semi-major and semi-minor axes of the melt pools represent this statistical measurement error combined with

systematic error introduced by fluctuations in the laser energy ($\sim 2.5\%$) between melting/solidification experiments that lead to small differences in the size of the melt pool. For the Al–4Cu and Al–3Si velocity measurements, this systematic error was, respectively, 1.0% and 1.25%, representing just the variation in laser fluence between experiments at low magnification that were used for the measurements.

RESULTS

Figure 1 presents time-delay sequences of images recorded during rapid solidification following pulsed-laser melting in (a) Al–4Cu and (b) Al–3Si thin films. Each row of images in Fig. 1 was recorded from a separate solidification experiment performed with initial delay times of $0 \mu\text{s}$, $20 \mu\text{s}$, or $40 \mu\text{s}$, as indicated under the first image of each row. A full sequence of 9 images spanned $20.4 \mu\text{s}$. The last image of each sequence shows that solidification was complete by the designated time (32.75 and $47.65 \mu\text{s}$ for, respectively, the Al–4Cu and Al–3Si alloy films). The initial grain size of the as-deposited films was on the order of the film thickness ($\sim 50\text{--}100 \text{ nm}$). This nanocrystalline grain structure was not resolved at the magnifications used to obtain the time-resolved images in Fig. 1. The melt pool, labeled in the $0\text{-}\mu\text{s}$ image of Fig. 1a, is the darker featureless region with low contrast in each image, relative to the contrast due to grain growth and crystallographic orientation displayed in the newly formed solid phase surrounding the melt pool. The solid–liquid interface is clearly evident in the images of Fig. 1, allowing for tracking of solidification front evolution with time.

In both the Al–4Cu and Al–3Si alloys, the solid–liquid interface appears sharp and morphologically planar, with no evidence of dendritic growth during rapid solidification. In the Al–4Cu alloy, the initial melt pool dimensions were $\sim 38 \mu\text{m}$ and $31 \mu\text{m}$ along the semi-major and semi-minor axes, respectively. Directional crystal growth commenced between 5.1 and $7.65 \mu\text{s}$, evidenced by the columnar grains that propagate radially inward, and was complete by $\sim 31 \mu\text{s}$. At the end of the rapid solidification process ($\sim 28\text{--}30 \mu\text{s}$), a morphological instability^{48,49} developed at the solid–liquid interface. This will be become more apparent subsequently. In the Al–3Si alloy, the initial melt pool dimensions were $\sim 42 \mu\text{m}$ and $33 \mu\text{m}$ along the major and minor axes, respectively. Directional crystal growth commenced between $7.65 \mu\text{s}$ and $10.2 \mu\text{s}$, again evidenced by the radial propagation of columnar grains, and was complete by $\sim 45 \mu\text{s}$.

Figure 2 shows plots of the time evolution of the (a) melt pool area, (b) semi-major, r_a , and semi-minor, r_b , axes of the melt pool, and (c) solidification front velocities along each axis, v_a and v_b , for both alloys, obtained directly from the time-resolved images of Fig. 1. Error bars were calculated as

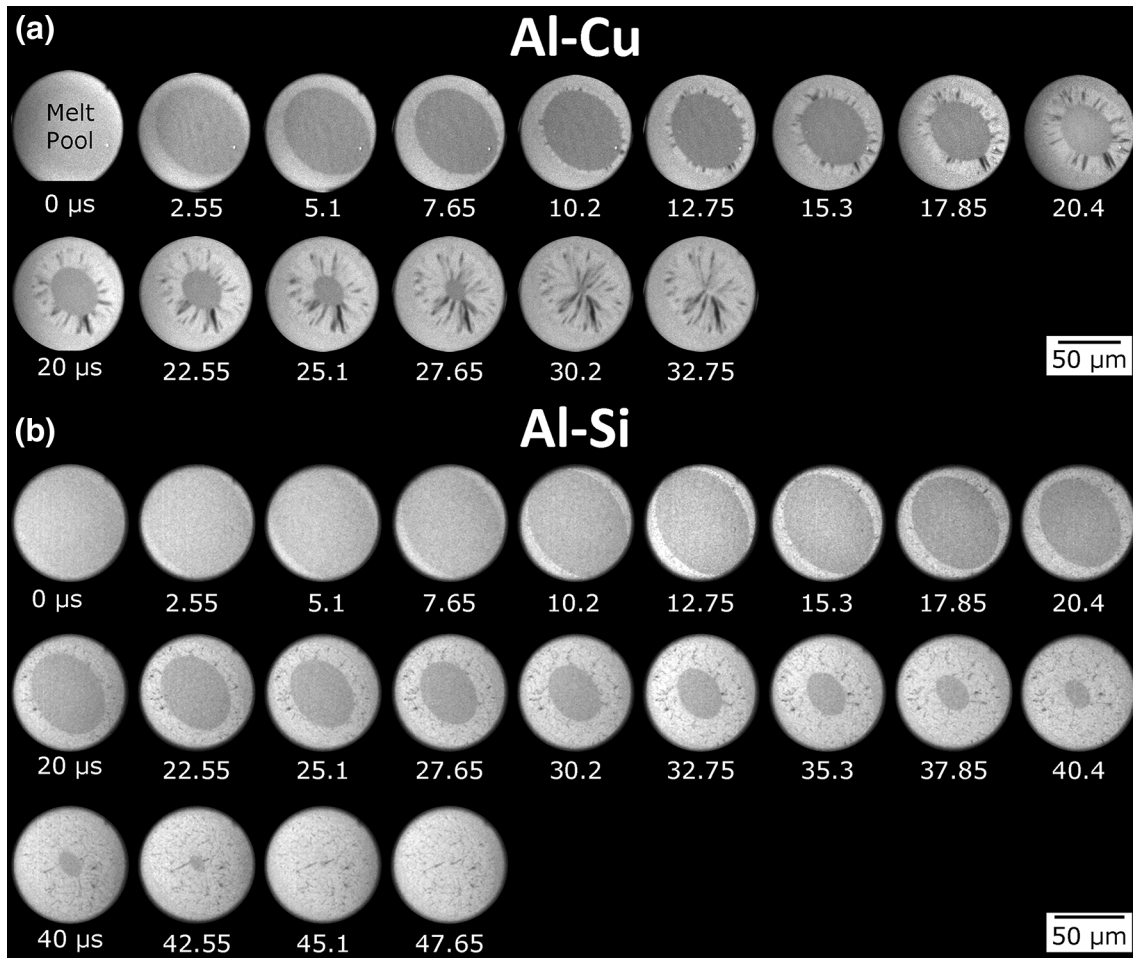


Fig. 1. Dynamic time-delay sequence of images recorded with low spatial resolution during rapid solidification in (a) Al-4Cu and (b) Al-3Si alloy thin films after pulsed-laser melting. The indicated times below each image are the delays (in μs) between the peak of the Gaussian laser pulse that melted the film and the 50-ns electron pulse used to form the image.

described in the “Experimental” section. The data for r_a and r_b for each alloy were fit to a second-order polynomial: $r = a_1 t^2 + a_2 t + a_3$. The coefficients and standard error of the coefficients are provided in Table I, along with values of R^2 and the mean absolute error for each fit. A major source of error in the polynomial fits arises from using multiple experiments to span the timeframe of rapid solidification for each alloy. Increasing the inter-frame temporal spacing to capture the entire rapid solidification event in a single experiment (i.e., a single movie mode acquisition) results in a reduction of data available for fitting with the potential to miss completely the onset of growth or growth-mode changes, which is why an inter-frame temporal spacing of $2.55 \mu\text{s}$ was chosen. In Fig. 2b, both r_a and r_b decrease monotonically with time during rapid solidification, and the rate of change is higher along r_a than along r_b . This is a consequence of the local curvature along the elliptical melt pool, leading to a higher rate of heat extraction along r_a , and has been confirmed by finite-element model calculations.⁵⁰ This also implies a range in the rate of

change of the axis length, and this is indicated in Fig. 2b by the gray shading between the polynomial curves for the time evolution of r_a and r_b , which will be the points of, respectively, maximum and minimum local curvature (and, hence, heat extraction) along the solid-liquid interface.

The polynomial expressions for the time evolution of r_a and r_b were differentiated with respect to time to obtain linear expressions for the velocity evolution with time along each axis, v_a and v_b . The solidification front velocities are plotted in Fig. 2c, where the gray shading now represents a range of velocities that depends on position along the solid-liquid interface. It is evident from the velocity plots that the solid-liquid interface accelerated as rapid solidification progressed. For the Al-4Cu alloy, v_a and v_b increased from, respectively, $\sim 0.67 \text{ m/s}$ and 0.55 m/s at $5.1 \mu\text{s}$ to $\sim 2.1 \text{ m/s}$ and 1.8 m/s at $30.2 \mu\text{s}$. For the Al-3Si alloy, v_a and v_b accelerated from, respectively, $\sim 0.78 \text{ m/s}$ and 0.60 m/s at $7.65 \mu\text{s}$ to $\sim 1.4 \text{ m/s}$ and 1.1 m/s at $45.1 \mu\text{s}$. As seen in Fig. 2c and using the values provided in Table I, the steady-state constant

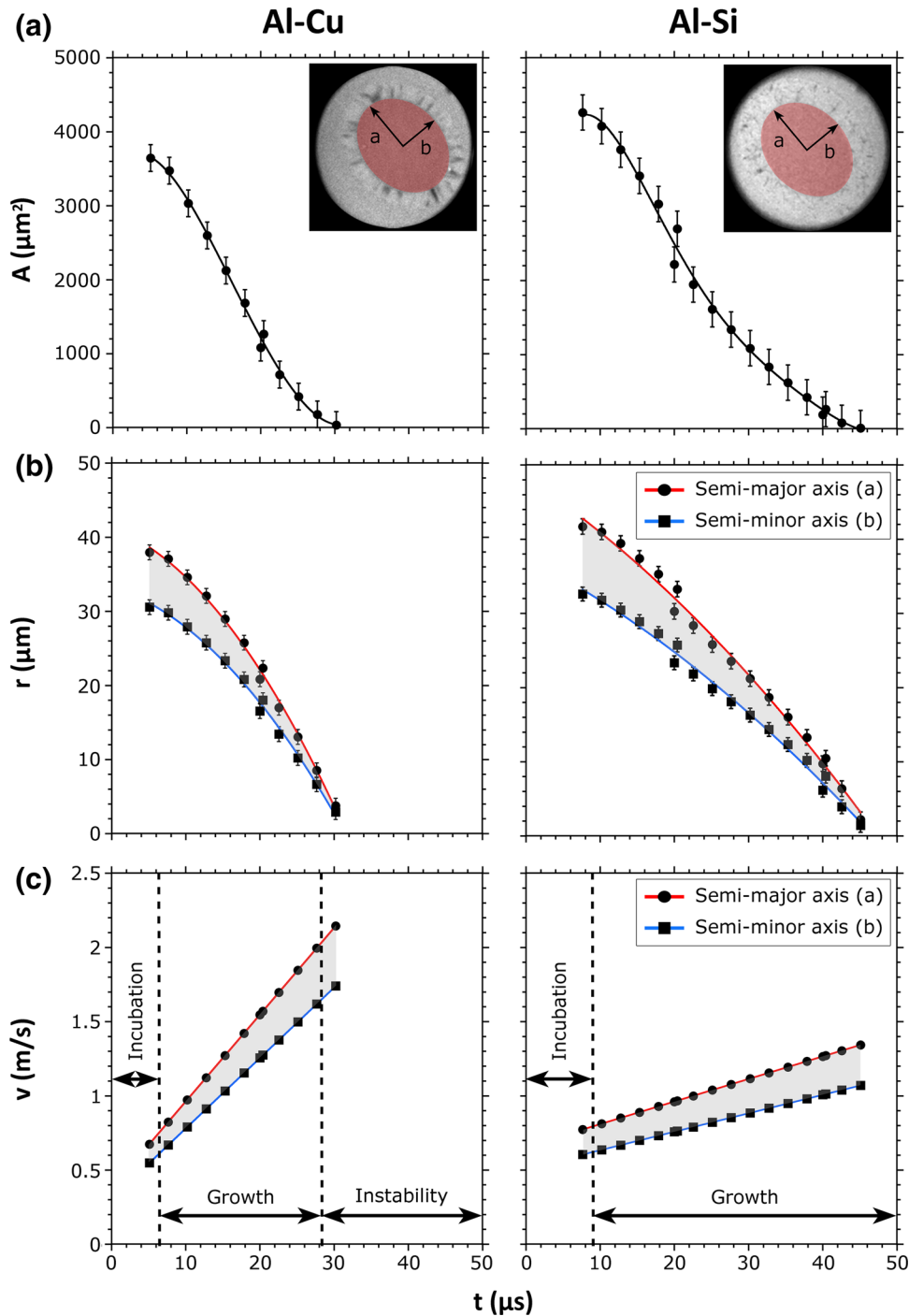


Fig. 2. For (left) Al-Cu and (right) Al-Si: time evolution of (a) area of the melt pool, (b) semi-major and semi-minor axes of the melt pool, and (c) solidification front velocity. The gray areas bounded by the semi-major and semi-minor axes in (b) and (c) represent, respectively, the ranges of axis length and velocity along the solid-liquid interface.

accelerations, α_a and α_b , were, respectively, $5.8 \times 10^4 \text{ m/s}^2$ and $4.8 \times 10^4 \text{ m/s}^2$ for Al-4Cu and $1.6 \times 10^4 \text{ m/s}^2$ and $1.2 \times 10^4 \text{ m/s}^2$ for Al-3Si. In both alloys, an initial rapid acceleration must have occurred prior to the steady-state growth mode of constant acceleration captured in the DTEM image sequences of Fig. 1, as all four of the linear

plots for the velocity evolution in Fig. 2c extrapolate back to negative times for zero velocity, which is unrealistic. This indicates that shorter inter-frame temporal spacings are required to capture this rapid initial acceleration and the transition to the steady-state constant acceleration during columnar growth.

Table I. Fitting parameters^a obtained for polynomial fits to the time evolution of the semi-major and semi-minor axes of Al-Cu and Al-Si melt pools

	Al-Cu						Al-Si					
	Major axis			Minor axis			Major axis			Minor axis		
Coefficients	a_1	a_2	a_3	a_1	a_2	a_3	a_1	a_2	a_3	a_1	a_2	a_3
Standard error	-0.029	-0.375	41.29	-0.024	-0.307	33.30	-0.008	-0.657	48.24	-0.006	-0.510	37.48
R^2	0.004	0.135	1.080	0.004	0.126	1.011	0.002	0.118	1.419	0.002	0.101	1.214
Mean absolute error	0.5927			0.4952			0.8138			0.7248		

^aThe experimental data were fit to a second-order polynomial: $r = a_1t^2 + a_2t + a_3$. The coefficients and standard error of the coefficients are provided in the table, along with values of R^2 and the mean absolute error for each fit.

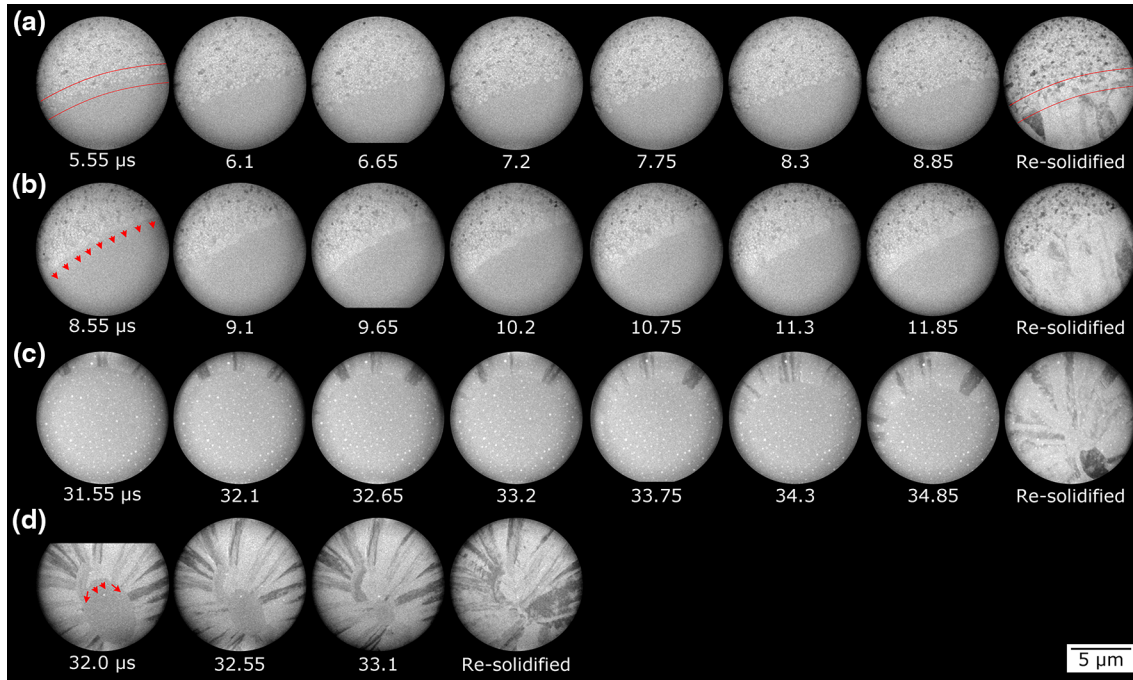


Fig. 3. Dynamic time-delay sequences of images recorded with higher spatial resolution during rapid solidification in an Al-4Cu thin-film alloy, showing (a) the transition from incubation to growth, (b) the early stages of columnar growth at the perimeter of the melt pool, (c) columnar growth near the center of the melt pool, and (d) instability at the solid-liquid interface and subsequent growth to the end of solidification. Images labeled Re-solidified were acquired minutes after the rapid solidification experiment. In (a), the red lines are meant to highlight the solid-liquid interface. The red arrows in (b) and (d) indicate the direction of growth.

The measured velocities can be related to the microstructure evolution seen in Fig. 1. In both alloys, growth commenced after an initial incubation period. In the Al-4Cu alloy, an instability at the solid-liquid interface led to a growth-mode transition at high velocity (~ 2 m/s). The approximate velocity ranges of these zones of the rapid solidification process are indicated on Fig. 2c. Using the low-magnification images of Fig. 1, the approximate timeframes for growth modes and growth-mode transitions were determined for each alloy, and time-resolved imaging experiments were conducted

using shorter inter-frame temporal spacings (appropriately chosen based on the measured solidification velocities of Fig. 2c) at higher magnification.

Figure 3 presents the growth modes and growth-mode transitions in the Al-4Cu alloy, showing (a) the transition from incubation to growth, (b) the early stages of columnar growth at the perimeter of the melt pool, (c) later stages of columnar growth near the center of the melt pool, and (d) instability at the solid-liquid interface and subsequent growth to the end of solidification. It should be noted that the small deviations in the times for the growth

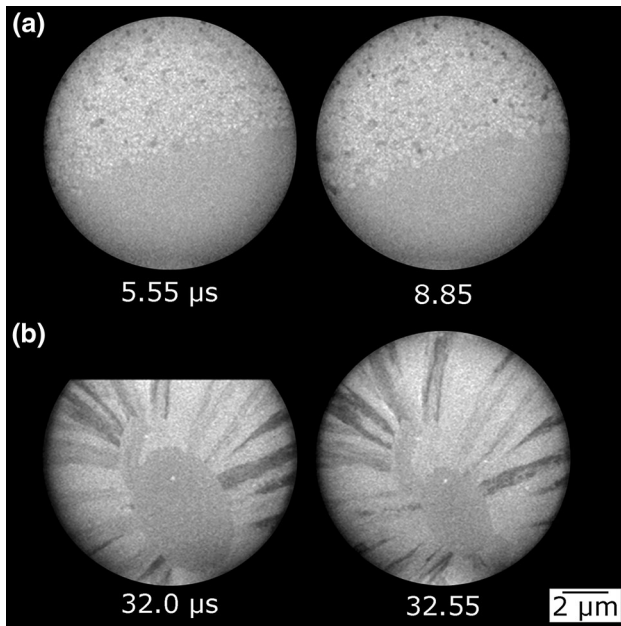


Fig. 4. Enlarged images from (a) Fig. 3a, b, and d, to more clearly show the growth-mode transitions from (a) incubation to growth and (b) columnar growth to instability development.

modes and growth-mode transitions relative to those of Fig. 1 are due to fluctuations in the laser energy used to produce the melt pools. During the incubation period prior to growth, small equiaxed grains (the region highlighted by the red lines in Fig. 3a) with random crystallographic orientations (evident from the contrast in the DTEM images, where darker grains were closer to a zone-axis orientation) developed along the perimeter of the melt pool. These grains were part of a larger heat-affected zone surrounding the initial melt pool that was the result of the Gaussian profile of the laser used to melt the alloy film. The transition to growth occurred when the equiaxed grains at the solid-liquid interface began to elongate along the direction of heat flow from the liquid to the solid phase (i.e., the radial direction, perpendicular to the solid-liquid interface), while slightly expanding in the direction parallel to the solid-liquid interface, which likely resulted from an undercooling due to Cu rejection from the grains at the solid-liquid interface. This elongation and expansion of the grains at the solid-liquid interface is more clearly seen in Fig. 4a, where the first and last images (5.55 μs and 8.85 μs) of the time-delay sequence of Fig. 3a are enlarged.

Columnar growth is evident in Fig. 3b and c. The red arrows in Fig. 3b indicate the crystal growth directions (radially inward). Measurements using Fig. 3b and c yield local velocities along the solidification front of, respectively, ~ 0.24 – 0.35 m/s during the early stages of columnar growth and ~ 0.76 – 0.84 m/s during the later stages of columnar growth. These velocities are consistent with the

range of values measured from low-magnification DTEM images of the entire melt pool (Fig. 2), as well as with observations and measurements of an accelerating solidification front. The lower velocity range (~ 0.24 – 0.35 m/s) measured during the early stages of growth also provides evidence for an initial rapid acceleration prior to the steady-state acceleration that developed during columnar growth, though further experimentation is ongoing with finer inter-frame temporal spacings (< 500 ns) to confirm this.

Figure 3d shows the transition from steady-state columnar growth to instability development along the solid-liquid interface. (Comparison with Figs. 1 and 2 reveal a small discrepancy between the times to instability and completion of solidification. This is a consequence of small fluctuations in laser energy between experiments.) A morphological instability at the solidification front occurred at a critical velocity, predicted to correspond to the velocity of absolute stability,^{48,49} leading to a banded morphology microstructure^{31,33,51,52} at the center of the rapidly solidified alloy melt pool. Interface velocity measurements (Fig. 2) determined that the instability occurred at ~ 2 m/s, which is consistent with previous ex situ velocity measurements and calculations^{31,33} for an Al-4Cu alloy. At this instability point, growth transitioned from an inward radial direction opposite that of heat flow to an oscillatory growth mode where the solidification front advanced simultaneously along directions both parallel and perpendicular to the isotherms of the elliptically-shaped melt pool, as indicated by the red arrows in Fig. 3d. In Fig. 4b, the 32.0- μs and 32.55- μs images of Fig. 3d appear enlarged, to illustrate more clearly this oscillatory growth mode. It is evident that the local curvature of the solid-liquid interface is much higher along the semi-major axis than along the semi-minor axis during instability evolution. In all in situ experiments for the Al-4Cu alloy, this morphological instability occurred in grains located along the semi-major axis. This is consistent with the higher heat extraction of the elliptically-shaped melt pools, which results in a higher solidification front velocity for interface segments along the semi-major axis (Fig. 2c).⁵⁰

Figure 5 presents HAADF STEM images acquired from the (a) edge and (b) center of the resolidified Al-4Cu melt pool, showing the microstructural zones and composition variations that developed during rapid solidification. The contrast in the HAADF-STEM images is primarily due to a dependence on atomic number, Z .⁵³ As observed in thin-film rapid solidification experiments with higher-Cu content Al-Cu alloys,¹⁷ the small-grained microstructure shown in Fig. 5a at the edge of the melt pool consists of a hypoeutectic structure, with equiaxed grains of proeutectic α -Al (dark contrast in the images) surrounded by a Cu-enriched θ -Al₂Cu phase (bright contrast in the images) at the boundaries of these grains. This hypoeutectic microstructure is

part of a larger heat-affected zone that resulted from the Gaussian profile of the laser heating pulse, where the temperature profile through the heat-affected zone decayed with distance from the edge of the melt pool from the melting temperature, T_m , through the mixed-phase ($\alpha + L$) region of the equilibrium phase diagram to the eutectic temperature, T_{eut} , and then to temperatures below T_{eut} . The microstructural coarsening and phase separation that produce this hypoeutectic microstructure, relative to the initial nanocrystalline grains of the as-deposited thin films, can be attributed to the initial heating with the laser pulse and subsequent transport of heat through the plane of the alloy film during all stages, but predominantly during the incubation period, of the rapid solidification process.

The transition from incubation to growth and the rapid acceleration associated with this transition can be related to the resultant microstructure. In the initial transition region of the Al–4Cu solidification microstructure (highlighted by the red lines in Fig. 5a), grains of α -Al solid solution grew with shapes elongated along the growth direction (opposite the direction of heat flow), clearly deviating from the equiaxed grain shape in the heat-affected zone surrounding the melt pool. The contrast changes in the HAADF-STEM images of Fig. 5a, where the darker contrast (Al-rich) transitions to a brighter contrast (increased Cu content) along the direction parallel to grain growth (radially inward) across ~ 500 nm, would be consistent with a composition change across this region and is likely due to rapid acceleration of the solid–liquid interface velocity that led to solute trapping^{54,55} under non-equilibrium growth conditions. This interpretation is consistent with the velocity measurements of Fig. 2, which indicate a rapid acceleration of the solidification front at the transition from incubation to directional crystal growth. This transition facilitates directional solidification of a non-equilibrium eutectic product, as inferred from the appearance of the Cu-enriched intragranular precipitates (bright contrast in Fig. 5). Prior work used selected-area diffraction patterns to determine that the Cu-enriched precipitates are consistent with θ -phase-related structures.^{56–59}

Growth then proceeded with a columnar morphology and steady-state acceleration to the point of absolute stability,^{48,49} as seen in Fig. 5a and b. This columnar grain morphology was a result of the polycrystalline state of the as-deposited film. The columnar grains, as shown in Figs. 1 and 3, advanced during growth with a planar, morphologically smooth solidification front until the onset of instability at the solid–liquid interface. A competitive growth process occurred during this steady-state acceleration, where a subset of columnar grains expanded laterally at a sufficiently rapid rate to occlude the growth of neighboring grains. This occlusion process was active during the entire

columnar growth stage, as evidenced by Fig. 5. Large elongated columnar grains extend from the edge to center of the melt pool, ranging in length from ~ 25 μm to 30 μm and width from ~ 0.5 μm to 3.5 μm with a thickness of 0.08 μm . The columnar grains are comprised of the intragranular non-equilibrium eutectic solidification product.¹⁷ Similar to the two-phase microstructure in the heat-affected zone, a continuous Cu-enriched phase was also present at the boundaries between all columnar grains (Fig. 5). This likely resulted from Cu rejection during rapid directional growth of the columnar grains of non-equilibrium eutectic. Higher curvature of the solid–liquid interface at boundaries between neighboring solidifying grains due to crystallographic misorientation would be expected to lead to rejection of Cu at these boundary junctions to produce the conditions for formation of this Cu-enriched phase.

Morphological instability at the solid–liquid interface occurred at a velocity of ~ 2 m/s (see Figs. 1 and 2), resulting in the large central region of the re-solidified microstructure shown in Fig. 5b. This microstructural region consists of a banded morphology common to many rapidly solidified alloys^{17,29,51,60–62} in which the solidification conditions reach a critical velocity that produces the interfacial instability.^{48,49} The banded morphology solidification microstructure is comprised of alternating bands of microsegregation-free, supersaturated solid solution α -Al, a product of partitionless crystal growth (composition analyses by EDS⁵⁸ have shown that these bands exhibit the nominal alloy composition, consistent with complete solute trapping), and bands of the same non-equilibrium eutectic micro-constituent present throughout the columnar grains. The banding was produced when the oscillatory instability initiated at a critical velocity (typically described as the point at which the solidification front velocity exceeds the diffusivity of solute in the liquid, and represented by a rapid increase of the velocity-dependent partition coefficient toward unity),⁶³ resulting in concurrent growth modes: radial growth of non-equilibrium eutectic product and partitionless growth of microsegregation-free α -Al along isothermal profiles within the melt pool. The evolution of this instability with concurrent growth modes was observed in the time-resolved imaging experiments and is shown in Figs. 3 and 4. It is also evident that the central banded structure formed from numerous grains, where columnar grains closest to the major axis of the elliptical melt pool (and hence, highest curvature along the melt pool with highest rate of heat extraction and solidification front velocity) expanded rapidly in a lateral direction along isotherms with a partitionless growth mode, forcing neighboring grains to grow laterally around these fastest-growing grains and preventing further growth of the large majority of columnar grains. Essentially, over a short timeframe, numerous

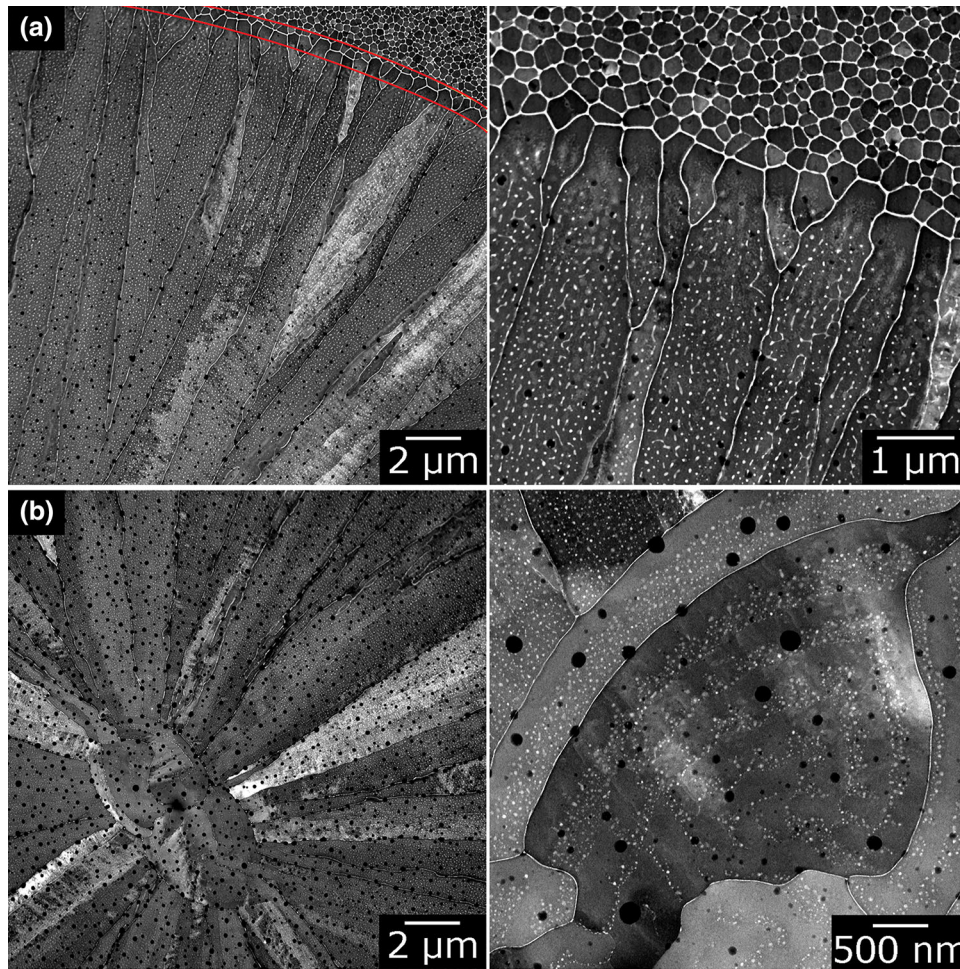


Fig. 5. HAADF STEM images acquired from the (a) edge and (b) center of a re-solidified Al-4Cu melt pool showing the microstructural zones and composition variations that developed during rapid solidification. The red lines in (a) along the perimeter of the re-solidified melt pool indicate the transition from incubation to growth. The presence of dark circular holes in the re-solidified film may be due to hydrogen outgassing of the amorphous silicon nitride substrates at high temperature.⁸⁰

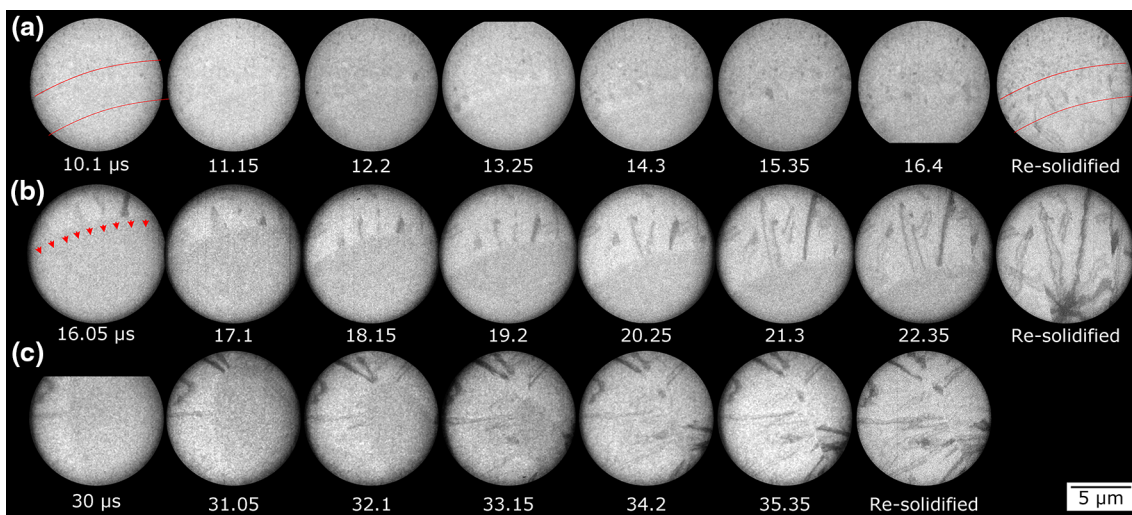


Fig. 6. Dynamic time-delay sequences of images recorded with higher spatial resolution during rapid solidification in an Al-3Si thin-film alloy, showing (a) the transition from incubation to the early stages of growth, (b) the early stages of columnar growth at the perimeter of the melt pool, and (c) columnar growth near the center of the melt pool. Images labeled Re-solidified were acquired minutes after the rapid solidification experiment. In (a), the red lines are meant to highlight the solid-liquid interface. The red arrows in (b) indicate the direction of growth.

different grains reached the critical conditions for the instability point to yield the central banded region of the rapidly solidified alloy microstructure.

In contrast to the composition segregation and instability that occurred during rapid solidification of the Al–4Cu alloy, rapid solidification in the Al–3Si alloy progressed with only a transition to columnar growth, as shown in Fig. 1. Figure 6 presents the growth modes and growth-mode transitions in the Al–3Si alloy, showing (a) the transition from incubation to growth, (b) the early stages of columnar growth at the perimeter of the melt pool, and (c) columnar growth near the center of the melt pool. As in Al–4Cu, the transition to growth in Al–3Si occurred when equiaxed grains at the solid–liquid interface began to elongate along the direction of heat flow from the liquid to the solid phase (i.e., the radial direction, perpendicular to the solid–liquid interface), while slightly expanding in the direction parallel to the solid–liquid interface. Columnar growth is evident in Figs. 6a–c, though clearly some of the contrast in these images is due to bend contours (see, for example, the “Re-solidified” image in Fig. 6b). The red arrows in Fig. 6b indicate the growth direction (radially inward) for the columnar morphology rapid solidification product. Measurements using Fig. 6 yield local velocities along the solidification front of, respectively, ~ 0.12 – 0.24 m/s during the early stages of columnar growth and ~ 0.49 – 1.0 m/s during the later stages of columnar growth, again consistent with the range of values measured from low-magnification DTEM images of the entire melt pool (Fig. 2), as well as with observations and measurements of an accelerating solidification front.

Figure 7 presents HAADF STEM images acquired from the (a) edge and (b, c) columnar growth and central regions of a re-solidified Al–3Si melt pool, showing the microstructural zones that developed during rapid solidification. In Fig. 7, a fine-scale structure is evident in the images (particularly in the higher-magnification images in the right column), indicative of small-grained precipitation throughout all regions of the microstructure. It is reasonable to assume that a supersaturated α -Al phase was formed during rapid solidification processing and, due to the mutual immiscibility of Al and Si, precipitation of Si occurred during post-solidification cooling. This has been observed in prior rapid solidification studies of Al–Si alloys³⁷ and has been shown to lead to increases in the hardness of Al–Si alloys after aging at relatively low temperatures for short times.⁶⁴

Based on the images in Fig. 6, coarsening with negligible compositional segregation occurred during incubation. During the transition from incubation to growth, grains of supersaturated α -Al solid solution grew with shapes elongated along the growth direction (opposite the direction of heat flow). Growth of supersaturated α -Al then proceeded with a columnar morphology and steady-state

acceleration to the completion of rapid solidification, with no instability at the solid–liquid interface. This columnar grain morphology was again a result of the polycrystalline state of the as-deposited film. Columnar grains, as shown in Figs. 1 and 6, advanced during growth with a planar, morphologically smooth solidification front. As with the Al–4Cu alloy, a competitive growth process was active during steady-state acceleration, leading to occlusion of grains that grew and expanded with slower rates. This occlusion process was active during the entire columnar growth stage, as evidenced in Figs. 6 and 7. Again, large elongated columnar grains extend from the edge to center of the melt pool, ranging in length from ~ 25 μm to 30 μm and width from ~ 0.5 μm to 4.5 μm with a thickness of 0.1 μm . In contrast to Al–Cu, the columnar grains terminate at the center of the melt pool along a distinct line, with a morphology similar to that of a weld centerline where grains curve toward this centerline with a degree that depends on proximity to the major axis of the elliptical melt pool. This is a result of an increasing rate of heat extraction with proximity to the major axis of the elliptically-shaped melt pool, due to higher local curvature as a function of position along the solid–liquid interface (see the time-resolved images of Fig. 1b).

DISCUSSION

In Situ Rapid Solidification Experiments with Al–Cu and Al–Si Alloys

The Al–Cu and Al–Si alloys investigated are hypoeutectic binary alloys with aluminum as the major constituent. The results show that the addition of solute, dependent on chemical species, leads to significant changes in rapid solidification behavior, resultant microstructure, and the presence of instabilities at the solidification front relative to similar processing conditions in pure Al.¹⁶ These differences can be understood in terms of relevant thermophysical parameters and solidification theory. Rapid solidification in both Al–Cu and Al–Si alloys has been studied extensively,^{17,27–33,36,37,57} and serve here as benchmark model systems for rapid solidification studies in nanoscale systems with planar thin-film geometries. It is a goal of the current research to extend the types of experimental observations and measurements performed here for the two model alloys to other relevant materials systems to further develop the scientific foundations underlying microstructure evolution during AM processing, while also informing and validating predictive modeling capabilities related to AM.

Incubation, the time between laser melting and initiation of rapid-solidification-related crystal growth, can be explained by considering the difference in laser absorptivity between the solid and liquid states of the alloys. Upon laser irradiation, there is a stepwise increase in the absorptivity of aluminum at the melting temperature,⁶⁵ where the

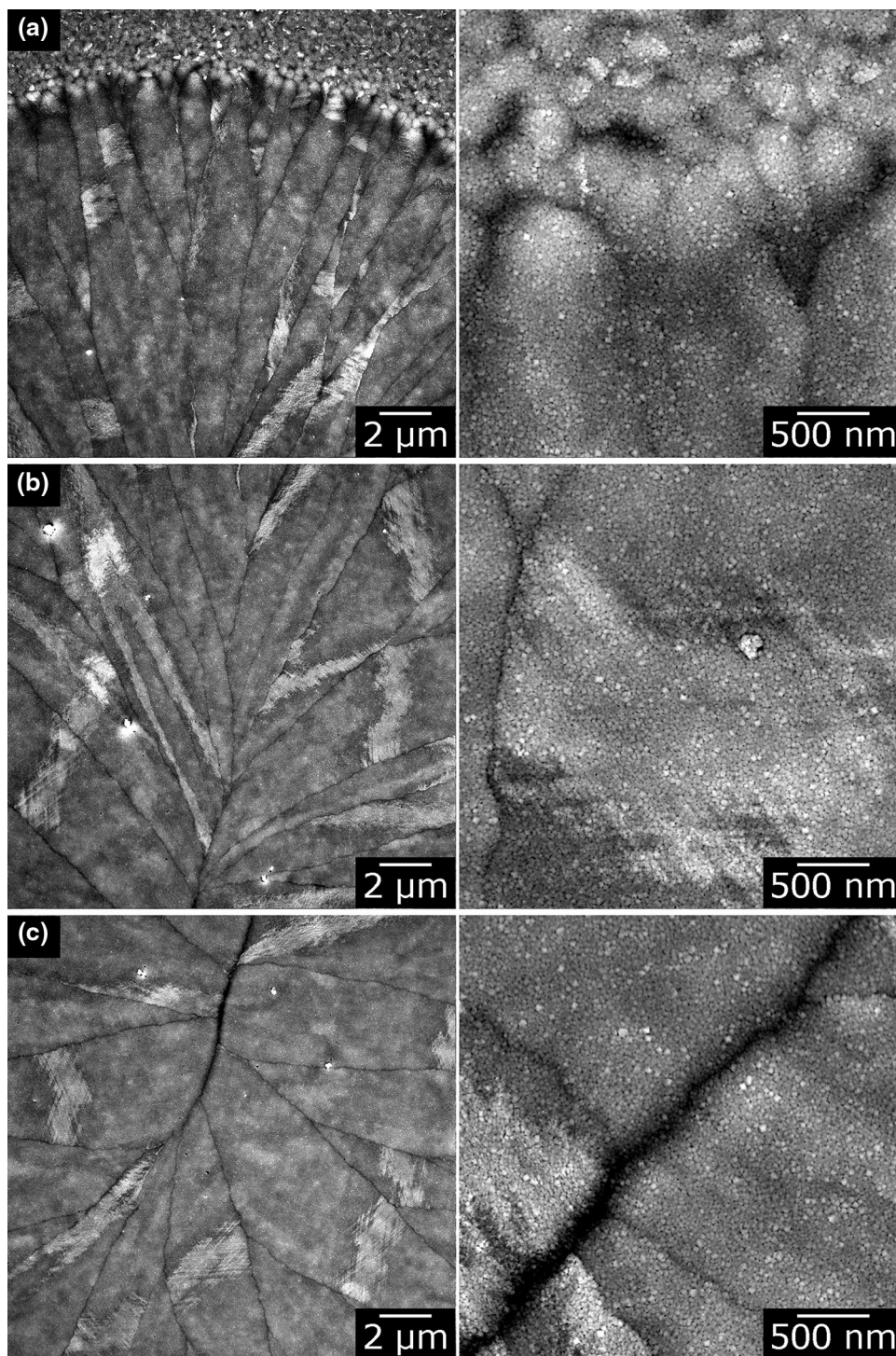


Fig. 7. HAADF STEM images acquired from the (a) edge and (b, c) columnar growth and central regions of a re-solidified Al-3Si melt pool showing the microstructural zones that developed during rapid solidification.

absorption by liquid aluminum is $\sim 1.5\text{--}2$ times greater^{65,66} than that of solid aluminum. Melting of the thin alloy films will occur at picosecond timescales⁶⁷ and commence at the upper surface of the films due to skin-depth effects. The liquid melt pool therefore absorbs significantly more energy

during the $\sim 15\text{-ns}$ laser irradiation, producing a steeper initial thermal gradient in the liquid melt pool relative to the surrounding solid film. The mixed-phase solid-liquid region (mushy zone) that develops at the perimeter of the melt pool after pulsed-laser melting can be expected to collapse

Table II. Materials used in experiments and corresponding thermophysical properties^{20–26}

Property	Symbol/units	Al-4Cu	Al-3Si	Amorphous SiN _x
Thermal conductivity	κ_s (W/m K) (solid)	190	121	10
	κ_l (W/m K) (liquid)	88	91	–
Latent heat of fusion	L (J/mol)	13.5	14.4	–
Solidus temperature	T_{sol} (K)	821	850	–
Liquidus temperature	T_{liq} (K)	903	918	–
Diffusion coefficient	D (m ² /s)	4.4×10^{-9}	2.6×10^{-9}	–
Partition coefficient	k	0.17	0.13	–
Gibbs–Thomson coefficient	Γ (m K)	1.0×10^{-6}	8.5×10^{-7}	–

quickly ($<1 \mu\text{s}$) based on thermal conductivities, heats of fusion, and estimated temperature gradients, as observed in the time-resolved images of Fig. 1, where the 0- μs images show a diffuse solid–liquid interface that was sharp and distinct by 2.55 μs . Incubation can therefore be characterized by rapid collapse of the mixed-phase region at the perimeter of the melt pool, followed by evolution toward thermal conditions at the solid–liquid interface that eventually favor directional crystal growth. At these temperatures ($\sim 630^\circ\text{C}$ and 645°C for, respectively, Al–4Cu and Al–3Si based on equilibrium phase diagrams),^{18,19} the thermal conductivities, κ , of both solid alloys are higher than the liquid alloys and an order of magnitude higher than that of the amorphous silicon nitride membranes (see Table II). Thus, as confirmed by numerical modeling for pure Al thin films,⁵⁰ heat conduction would be expected predominantly through the plane of the solid alloy film during cooling. The slightly longer incubation time in the Al–3Si alloy can be attributed to small differences in thermal conductivity, latent heat of fusion, and solute diffusivity in the liquid alloys (lower solid thermal conductivity, κ_s , and diffusivity, D , and higher latent heat, L , in Al–3Si relative to Al–4Cu), combined with solute rejection that produced a constitutionally undercooled boundary layer at the solid–liquid interface more readily in Al–4Cu.

Columnar growth was evident in both alloys during steady-state acceleration of the solid–liquid interface, with obvious differences in solidification product. In Al–4Cu, a non-equilibrium eutectic structure developed (Fig. 5a) while Al–3Si solidified with a supersaturated α -Al structure (Fig. 7a). Both solidification modes are consistent with prior rapid solidification studies of hypoeutectic Al–Cu and Al–Si alloys.^{30,31,33,35,36,57,68,69} In the Al–4Cu thin-film alloy, the observed eutectic structure is consistent with predictions of eutectic solidification modes in hypoeutectic alloys for high solidification front velocities,^{70–74} in which the cellular/dendrite tip temperature decreases as velocity increases, the temperature gradient does not significantly affect this reduction in tip temperature, and the undercooling at the interface becomes proportional to the square root of the solid–liquid interface velocity.

This implies increased undercooling at the accelerating solidification front and conditions where growth proceeds by a kinetically preferred eutectic. A coupled zone, or velocity-dependent extension of the range for eutectic growth, has been established for hypoeutectic Al-rich alloys in terms of a competitive growth model,⁷² where eutectic solidification can occur at compositions other than the thermodynamic eutectic composition.^{73,74} An entirely eutectic microstructure can be kinetically preferred rather than simultaneous growth of primary dendrites and interdendritic eutectic. The coupled zone typically expands and shifts its composition range as the velocity and undercooling increase, representing an undercooled compositional region where eutectic solidification product grows more rapidly than dendrites of either of the two terminal phases. Therefore, at the measured velocities of the solidification front in hypoeutectic Al–4Cu, it can be expected that the kinetically modified eutectic growth mode becomes dominant over cellular or dendritic growth modes. In the case of Al–3Si, this coupled zone had been shown to be skewed toward higher Si concentrations due to more sluggish growth kinetics of the faceted Si phase in the eutectic.^{35,36,69,74,75} Therefore, at the composition (Al–3Si) and solid–liquid interface velocities of this study, growth of supersaturated α -Al can be expected and is consistent with prior studies.³⁶

Columnar growth continued to the point of absolute stability in Al–4Cu, while the velocity reached in Al–3Si did not reach this critical limit. The velocity of absolute stability, v_{abs} , can be calculated by the expression:^{32,49}

$$v_{abs} = \frac{\Delta T_0 D}{k\Gamma} \quad (1)$$

where ΔT_0 is the temperature difference between the solidus and liquidus at the composition of interest, D is the diffusion coefficient of solute in the liquid, k is the partition coefficient, and Γ is the Gibbs–Thomson coefficient. Using the values provided in Table II, theoretical values of v_{abs} for Al–4Cu and Al–3Si are, respectively, 2.1 m/s and 1.6 m/s. These values agree with the time-resolved in situ observations of rapid solidification (Fig. 1) and associated velocity measurements (Fig. 2). The

onset of instability in the Al–4Cu alloy was measured to be ~ 2 m/s with a maximum velocity of 2.2 m/s along the major axis of the melt pool, while instability was not observed in the Al–3Si alloy with a maximum velocity of 1.1 m/s along the major axis (below the absolute stability limit).

Based on the time-resolved images of Figs. 1a and 3c, the tip radii of the rapidly solidifying eutectic columnar grains in the Al–4Cu alloy were large and nearly planar, consistent with models⁷⁶ that indicate that the solid–liquid interface close to the absolute stability limit should consist of morphologically flat-topped cells. The microsegregation-free bands in the banded morphology (Fig. 5b) can be attributed to the solidification front velocity reaching the absolute stability limit and ensuing partitionless solidification. This instability leads to concurrent partitionless solidification along isotherms in the melt pool and kinetically modified eutectic solidification along the radial direction of the thermal gradient, as shown in Figs. 3 and 4. As partitionless solidification advances along isotherms and over small radial distances, solute is no longer rejected into the liquid, leading to a deceleration (reduced undercooling) radially along the thermal gradient that drives the interface velocity back below v_{abs} and generates the eutectic solidification product again. This instability will be oscillatory, as both the velocity and undercooling (temperature) will fluctuate, yielding periodic variation in the growth modes⁴⁸ and the observed banded morphology of the solidification product microstructure. While this banding phenomenon has been studied extensively,^{17,29,31–33,51,52,62,77–79} the images in Figs. 3 and 4 represent the first in situ observations of this instability evolution with time, clearly showing the concurrent growth of partitionless and eutectic bands.

Implications for Additive Manufacturing

The ability to directly image the solid–liquid interface as it evolves in time using in situ TEM provides unique experimental insight to rapid solidification, and hence processes responsible for microstructure development during AM, that cannot be obtained with other characterization techniques. The applicability of the in situ time-resolved imaging experiments relies on matching the solidification conditions to those of AM processes. During solidification, the morphology of the solid–liquid interface and spatial scale of the developing microstructure are dictated by the thermal gradient and the solidification front velocity.⁷⁴ In these studies, as in AM processes, a thermal gradient across the solid–liquid interface is imposed by the laser beam profile and energy and absorptivity of the material that is being melted. Currently, the capability to measure the temperature and thermal gradient during these in situ rapid solidification experiments is lacking, though finite-element

simulations indicate extremely high gradients of the order of 10^6 – 10^7 K/m, such that rapid solidification occurred in these Al–Cu and Al–Si with high velocity in a large temperature gradient. This is consistent with the spatial scales of the observed microstructures and planar morphology of the solidification fronts during rapid solidification. However, this highlights the need for in situ sensors and diagnostics to monitor the temperature evolution with high spatial, temporal, and spectral resolutions. Techniques to accomplish this are the focus of ongoing work with the DTEM, and these types of measurements are needed for real-time control of AM processes.²

The in situ DTEM experiments were also carried out in nanoscale, thin-film alloy systems, yielding directional 2D solidification due to this experimental geometry. AM processes such as SLM employ metal and alloy powders and rapid solidification does not involve such small, controlled melt pool geometries. Yet the microstructures and spatial scales that develop will still be dictated, in both cases, by the temperature gradient and solidification front velocity. Comparisons with ex situ rapid solidification experiments involving laser surface melting in bulk Al–Cu alloys,^{31,33} in which microstructure selection maps were developed to correlate microstructure to growth velocity and alloy composition, reveal that the observed microstructures, measured velocities, and growth-mode transitions in thin-film Al–Cu alloys are consistent with these microstructure selection maps. This implies that thin-film effects are negligible and confirms the validity and applicability of these experimental results to AM processes. Extension of these experiments to new materials systems, particularly higher melting-point alloys, such as stainless steel and Ti-based alloys relevant to AM applications, are ongoing.

The significance of these data acquired from in situ experiments to AM relies on integration with modeling capabilities. Input from in situ experiments can be used to both inform and validate models that seek to predict microstructure evolution during AM processing. This integration of experiment and modeling is critical to improved understanding of processing-microstructure-properties/performance relationships, in order to advance AM toward a broadly used manufacturing tool.

CONCLUSION

Time-resolved measurements were obtained during rapid solidification in hypoeutectic Al–Cu and Al–Si thin-film alloys using dynamic transmission electron microscopy. In situ imaging of the solidification front enabled velocity measurements for the solidification front and confirmed a range of interface velocities, with maximum and minimum velocities along, respectively, the semi-major and semi-minor axes of the elliptical melt pool. This was a

consequence of heat extraction due to variations in the local curvature of the solid–liquid interface. In both alloys, after an initial incubation time of several microseconds, a columnar microstructure developed during acceleration of the solid–liquid interface. In the Al–Si alloy, columnar growth of supersaturated primary α -Al phase persisted to the end of the rapid solidification process. In the Al–Cu alloy, columnar growth of a non-equilibrium eutectic solidification product proceeded to the point of absolute stability at the solid–liquid interface, where a banded morphology common to many rapidly solidified alloys developed. In situ imaging provided the first direct observations of the evolution of this banded microstructure at this instability point.

These types of in situ measurements have broad implications for additive manufacturing through integration with predictive modeling capabilities. The results can both inform and validate models with the goal of understanding processing–microstructure–properties/performance relationships in additive manufacturing and non-equilibrium materials processing.

ACKNOWLEDGEMENTS

This work was performed under the auspices of the U.S. Department of Energy, by Lawrence Livermore National Laboratory (LLNL) under Contract No. DE-AC52-07NA27344. Activities and personnel at LLNL were supported by the U.S. Department of Energy, Office of Science, Office of Basic Energy Sciences, Division of Materials Science and Engineering under FWP SCW0974. Activities and personnel at the University of Pittsburgh received support from the National Science Foundation, Division of Materials Research, Metals & Metallic Nanostructures program through Grant No. DMR 1105757. Work at Los Alamos National Laboratory (LANL) was performed under the auspices of the U.S. Department of Energy by Los Alamos National Security, LLC, under Contract No. DE-AC52-06NA25396. Activities and personnel at LANL were supported by AJC's Early Career Award from the U.S. Department of Energy, Office of Science, Office of Basic Energy Sciences, Division of Materials Science and Engineering. DTEM sample preparation at LANL was performed at the Center for Integrated Nanotechnologies, an Office of Science User Facility operated for the U.S. Department of Energy, Office of Science.

REFERENCES

1. W.E. King, *JOM* 66, 2202 (2014).
2. M. Mani, B. Lane, A. Donmez, S. Feng, S. Moylan and R. Fesperman, in *Measurement Science Needs for Real-Time Control of Additive Manufacturing Powder Bed Fusion Processes*, NISTIR 8036 (National Institute of Standards and Technology, 2015), <http://dx.doi.org/10.6028/NIST.IR.8036>.
3. P.C. Collins, C.V. Haden, I. Ghamarian, B.J. Hayes, T. Ales, G. Penso, V. Dixit, and G. Harlow, *JOM* 66, 1299 (2014).
4. J. Gockel, J. Beuth, and K. Taminger, *Addit. Manuf.* 1–4, 119 (2014).
5. N.E. Hodge, R.M. Ferencz, and J.M. Solberg, *Comput. Mech.* 54, 33 (2014).
6. C. Karmath, B. El-dasher, G.F. Gallegos, W.E. King, and A. Sisto, *Int. J. Adv. Manuf. Technol.* 74, 65 (2014).
7. S.A. Khairallah and A. Anderson, *J. Mater. Process. Technol.* 214, 2627 (2014).
8. R. Martukanitz, P. Michaleris, T. Palmer, T. DebRoy, Z.-K. Liu, R. Otis, T.-W. Heo, and L.-Q. Chen, *Addit. Manuf.* 1–4, 52 (2014).
9. P. Michaleris, *Finite Elem. Anal. Des.* 86, 51 (2014).
10. P. Prabhakar, W.J. Sames, R. Dehoff, and S.S. Babu, *Addit. Manuf.* 7, 83 (2014).
11. T.I. Zohdi, *Comput. Mech.* 54, 171 (2014).
12. D.M. Herlach, *Mater. Sci. Eng. R* 12, 177 (1994).
13. J.E. Kline and J.P. Leonard, *Appl. Phys. Lett.* 86, 201902 (2005).
14. R. Zhong, A. Kulovits, J.M.K. Wiezorek, and J.P. Leonard, *Appl. Surf. Sci.* 256, 105 (2009).
15. A. Kulovits, R. Zhong, J.M.K. Wiezorek, and J.P. Leonard, *Thin Solid Films* 517, 3629 (2009).
16. A. Kulovits, J.M.K. Wiezorek, T. LaGrange, B.W. Reed, and G.H. Campbell, *Phil. Mag. Lett.* 91, 287 (2011).
17. J.T. McKeown, A.K. Kulovits, C. Liu, K. Zweigacker, B.W. Reed, T. LaGrange, J.M.K. Wiezorek, and G.H. Campbell, *Acta Mater.* 65, 56 (2014).
18. J.L. Murray, *Al–Cu Phase Diagram ASM Phase Diagrams Database*, P. Villars, ed.-in-chief, H. Okamoto and K. Cenzual, section eds., <http://www1.asminternational.org/ASMEnterprise/APD> (Materials Park, OH: ASM International, 2006).
19. J.L. Murray, *Al–Si Phase Diagram, ASM Phase Diagrams Database*, P. Villars, ed.-in-chief, H. Okamoto and K. Cenzual, section eds., <http://www1.asminternational.org/ASMEnterprise/APD> (Materials Park, OH: ASM International, 2006).
20. C.A. Muojekwu, I.V. Samarasekera, and J.K. Brimacombe, *Metall. Mater. Trans. B* 26, 361 (1995).
21. D.R. Poirier and E. McBride, *Mater. Sci. Eng. A* 224, 48 (1997).
22. Y. Du, Y.A. Chang, B. Huang, W. Gong, Z. Jin, H. Xu, Z. Yuan, Y. Liu, Y. He, and F.-Y. Xie, *Mater. Sci. Eng. A* 363, 140 (2003).
23. O.L. Rocha, C.A. Siqueira, and A. Garcia, *Metall. Mater. Trans. A* 34, 995 (2003).
24. M.D. Peres, C.A. Siqueira, and A. Garcia, *J. Alloys Compd.* 381, 168 (2004).
25. B.L. Zink and F. Hellman, *Solid State Commun.* 129, 199 (2004).
26. P.A.D. Jácome, M.C. Landim, A. Garci, A.F. Furtado, and I.L. Ferreira, *Thermochim. Acta* 523, 142 (2011).
27. M. Zimmermann, M. Carrard, and W. Kurz, *Acta Metall.* 37, 3305 (1989).
28. M. Zimmermann, A. Karma, and M. Carrard, *Phys. Rev. B* 42, 833 (1990).
29. M. Zimmermann, M. Carrard, M. Gremaud, and W. Kurz, *Mater. Sci. Eng. A* 134, 1278 (1991).
30. S.C. Gill, M. Zimmermann, and W. Kurz, *Acta Metall. Mater.* 40, 2895 (1992).
31. S.C. Gill and W. Kurz, *Acta Metall. Mater.* 41, 3563 (1993).
32. S.C. Gill and W. Kurz, *Mater. Sci. Eng. A* 173, 335 (1993).
33. S.C. Gill and W. Kurz, *Acta Metall. Mater.* 43, 139 (1995).
34. A. Prasad, H. Henein, E. Maire, and C.-A. Gandin, *Metall. Mater. Trans. A* 37A, 249 (2006).
35. H.A.H. Steen and A. Hellawell, *Acta Metall.* 20, 363 (1972).
36. M. Pierantoni, M. Gremaud, P. Magnin, D. Stoll, and W. Kurz, *Acta Metall. Mater.* 40, 1637 (1992).
37. Y. Birol, *J. Mater. Sci.* 31, 2139 (1996).
38. F.A. Espana, V.K. Balla, and A. Bandyopadhyay, *Phil. Mag.* 91, 574 (2011).
39. W.E. King, G.H. Campbell, A. Frank, B. Reed, J.F. Schmerge, B.J. Siwick, B.C. Stuart, and P.M. Weber, *J. Appl. Phys.* 97, 111101 (2005).

40. J.S. Kim, T. LaGrange, B.W. Reed, M. Taheri, M.R. Armstrong, W.E. King, N.D. Browning, and G.H. Campbell, *Science* 321, 1472 (2008).
41. T. LaGrange, G.H. Campbell, B.W. Reed, M. Taheri, J.B. Pesavento, J.S. Kim, and N.D. Browning, *Ultramicroscopy* 108, 1441 (2008).
42. B.W. Reed, M.R. Armstrong, N.D. Browning, G.H. Campbell, J.E. Evans, T. LaGrange, and D.J. Masiel, *Microsc. Microanal.* 15, 272 (2009).
43. T. LaGrange, B.W. Reed, M.K. Santala, J.T. McKeown, A. Kulovits, J.M.K. Wiezorek, L. Nikolova, F. Rosei, B.J. Siwick, and G.H. Campbell, *Micron* 43, 1108 (2012).
44. G.H. Campbell, J.T. McKeown, and M.K. Santala, *Appl. Phys. Rev.* 1, 041101 (2014).
45. T. LaGrange, B.W. Reed, and D.J. Masiel, *MRS Bull.* 40, 22 (2015).
46. W.S. Rasband, ImageJ, U.S. National Institutes of Health, Bethesda, MD, USA, <http://imagej.nih.gov/ij/>, 1997–2014.
47. C.A. Schneider, W.S. Rasband, and K.W. Eliceiri, *Nat. Methods* 9, 671 (2012).
48. S.R. Coriell and R.F. Sekerka, *J. Cryst. Growth* 61, 499 (1983).
49. W.W. Mullins and R.F. Sekerka, *J. Appl. Phys.* 35, 444 (1964).
50. C. Liu, K. Zwiack, J.T. McKeown, T. LaGrange, B.W. Reed, G.H. Campbell, and J.M.K. Wiezorek, *Microsc. Microanal.* 21, 811 (2015).
51. M. Carrard, M. Gremaud, M. Zimmermann, and W. Kurz, *Acta Metall. Mater.* 40, 983 (1992).
52. A. Karma and A. Sarkissian, *Phys. Rev. Lett.* 68, 2616 (1992).
53. S.J. Pennycook, *Ultramicroscopy* 30, 58 (1989).
54. J.C. Baker and J.W. Cahn, *Acta Metall.* 17, 575 (1969).
55. P.M. Smith and M.J. Aziz, *Acta Metall. Mater.* 42, 3515 (1994).
56. J.L. Murray, *Int. Met. Rev.* 30, 211 (1985).
57. R.K. Singh, K. Chattopadhyay, S. Lele, and T.R. Anantharaman, *J. Mater. Sci.* 17, 1617 (1982).
58. K. Zwiack, *In-Situ TEM Investigations of Rapid Solidification of Aluminum Copper Alloys*, Ph.D. Thesis, University of Pittsburgh, 2015.
59. K. Zwiack, M.A. Gordillo, C. Liu, J.T. McKeown, T. LaGrange, B.W. Reed, G.H. Campbell, and J.M.K. Wiezorek, *Microsc. Microanal.* 21, 1465 (2015).
60. W.J. Boettinger, D. Shechtman, R.J. Schaefer, and F.S. Biancaniello, *Metall. Trans. A* 15A, 55 (1984).
61. W. Kurz and R. Trivedi, *Acta Metall. Mater.* 38, 1 (1990).
62. M. Gremaud, M. Carrard, and W. Kurz, *Acta Metall. Mater.* 39, 1431 (1991).
63. M.J. Aziz and T. Kaplan, *Acta Metall.* 36, 2335 (1988).
64. M. Gupta and S. Ling, *J. Alloys Compd.* 287, 284 (1999).
65. A.M. Prokhorov, V.I. Konov, I. Ursu and I.N. Mihailsecu, *Laser Heating of Metals* (Adam Hilger, IOP Publishing Ltd., Philadelphia, 1990), pp. 34–36.
66. S.B. Boyden and Y. Zhang, *J. Thermophys. Heat Tran.* 20, 9 (2006).
67. B.J. Siwick, J.R. Dwyer, R.E. Jordan, and R.J.D. Miller, *Science* 302, 1382 (2003).
68. D.B. Williams and J.W. Edington, *J. Mater. Sci.* 12, 126 (1977).
69. O.A. Atasoy, F. Yilmaz, and R. Elliott, *J. Cryst. Growth* 66, 137 (1984).
70. M.H. Burden and J.D. Hunt, *J. Cryst. Growth* 22, 99 (1974).
71. M.H. Burden and J.D. Hunt, *J. Cryst. Growth* 22, 109 (1974).
72. M.H. Burden and J.D. Hunt, *J. Cryst. Growth* 22, 328 (1974).
73. W.J. Boettinger, in *Rapidly Solidified Amorphous and Crystalline Alloys*, B.H. Kear, B.C. Giessen and M. Cohen, eds. (New York: Elsevier Science Publishing Co., Inc., 1982).
74. W. Kurz and D.J. Fisher, *Fundamentals of Solidification* (Switzerland: Trans Tech SA, 1984).
75. J.A. Dantzig and M. Rappaz, *Solidification* (Lausanne: EPFL Press, 2009).
76. W. Kurz and D.J. Fisher, *Acta Metall.* 29, 11 (1981).
77. G.J. Merchant and S.H. Davis, *Acta Metall. Mater.* 38, 2683 (1990).
78. M. Conti, *Phys. Rev. E* 58, 6166 (1998).
79. M. Conti, *Phys. Rev. E* 58, 6101 (1998).
80. J. Yota, J. Hander, and A.A. Saleh, *J. Vac. Sci. Technol. A* 18, 372 (2000).